

# Crustal and uppermost mantle structure in southern Africa revealed from ambient noise and teleseismic tomography

Yingjie Yang<sup>1</sup>, Aibing Li<sup>2</sup> and Michael H. Ritzwoller<sup>1</sup>

<sup>1</sup>Center for Imaging the Earth's Interior, Department of Physics, University of Colorado at Boulder, Boulder, CO 80309-0390, USA.

E-mail: yingjie.yang@colorado.edu

<sup>2</sup>Geosciences Department, University of Houston, Houston, TX 77204-5007, USA

Accepted 2008 March 3. Received 2008 March 3; in original form 2007 August 2

## SUMMARY

Rayleigh wave phase velocity maps in southern Africa are obtained at periods from 6 to 40 s using seismic ambient noise tomography applied to data from the Southern Africa Seismic Experiment (SASE) deployed between 1997 and 1999. These phase velocity maps are combined with those from 45 to 143 s period which were determined previously using a two-plane-wave method by Li & Burke. In the period range of overlap (25–40 s), the ambient noise and two-plane-wave methods yield similar phase velocity maps. Dispersion curves from 6 to 143 s period were used to estimate the 3-D shear wave structure of the crust and uppermost mantle on a  $1^\circ \times 1^\circ$  grid beneath southern Africa to a depth of about 100 km. Average shear wave velocity in the crust is found to vary from  $3.6 \text{ km s}^{-1}$  at 0–10 km depths to  $3.86 \text{ km s}^{-1}$  from 20 to 40 km, and velocity anomalies in these layers correlate with known tectonic features. Shear wave velocity in the lower crust is on average low in the Kaapvaal and Zimbabwe cratons and higher in the surrounding Proterozoic terranes, such as the Limpopo and the Namaqua-Natal belts, which suggests that the lower crust underlying the Archean cratons is probably less mafic than beneath the Proterozoic terranes. Crustal thickness estimates agree well with a previous receiver function study of Nair *et al.*. Archean crust is relatively thin and light and underlain by a fast uppermost mantle, whereas the Proterozoic crust is thick and dense with a slower underlying mantle. These observations are consistent with the southern African Archean cratons having been formed by the accretion of island arcs with the convective removal of the dense lower crust, if the foundering process became less vigorous in arc environments during the Proterozoic.

**Key words:** Surface waves and free oscillations; Seismic tomography; Cratons.

## INTRODUCTION

Southern Africa consists of two of the oldest continental blocks on Earth, the Kaapvaal and Zimbabwe cratons, and several Proterozoic mobile belts surrounding the two cratons (Fig. 1). The Kaapvaal craton comprises a number of geological terranes with the oldest blocks in the eastern parts of the craton and the youngest in the western parts (de Wit *et al.* 1992). It was assembled over a 1 Ga period before 2.6 Ga. Between 2.0 and 2.8 Ga, the Kaapvaal craton collided with the Zimbabwe craton to the north, forming the Limpopo orogenic belt. Mobile belts accreted near the margins of the two cratons in the mid- to late-Proterozoic. The Kaapvaal craton is bounded by the Namaqua-Natal belt on the south and by the Kheiss thrust belt on the west. The Zimbabwe craton is surrounded by the Okwa/Magondi terrane in the west. The Bushveld event at 2.05 Ga (de Wit *et al.* 1992) disrupted the stable Kaapvaal craton and formed the Bushveld Complex in the northern Kaapvaal craton.

The Phanerozoic Cape Fold belt (0.3 Ga) is the youngest part of southern Africa.

Southern Africa has long been a target for multidisciplinary scientific studies because the region holds much information about the early history of the Earth. The seismic structures of the crust and upper mantle in southern African, especially in the cratons, provide essential constraints on the formation and evolution of early Earth. For example, both global and regional seismic tomography (Ekstrom *et al.* 1997; Grand *et al.* 1997; Ritsema & van Heijst 2000) found that the Kaapvaal craton is characterized by a fast and thick lithosphere, which has helped to stabilize the craton over geological history without suffering severe deformation by intense nearby tectonic activities.

In order to study the formation and evolution of cratons in more detail in southern Africa, the Southern Africa Seismic Experiment project (hereafter referred to as SASE) was deployed between 1997 and 1999. SASE is a large-scale broad-band seismic array designed

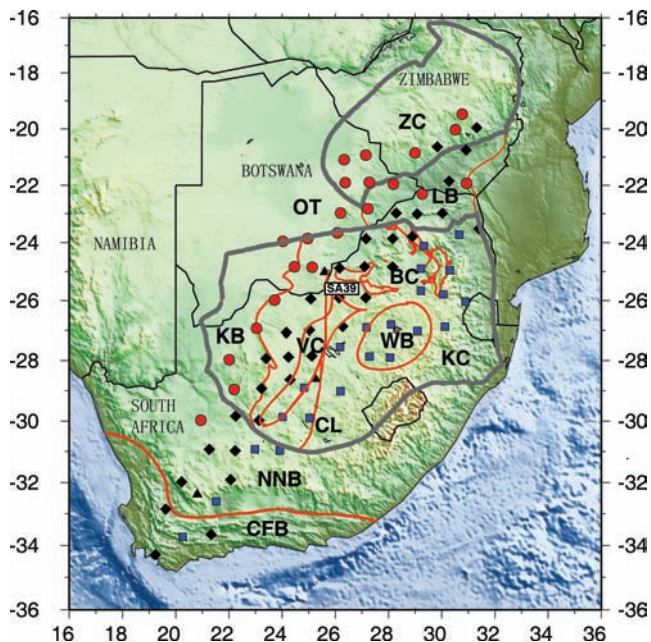


**Figure 1.** Map of topography, seismic stations, and tectonic regions in southern Africa. Diamonds are stations that operated for 2 yr. Stations at the circles were moved to the sites marked by squares after 1 yr of operation. Triangles are long-term stations. The two cratons are outlined by grey lines: KC, Kaapvaal Craton; ZC, Zimbabwe Craton. Proterozoic provinces are outlined by red lines: BC, Bushveld Complex; VC, Ventersdorp Complex; WB, Witwatersrand Basin; LB, Limpopo Belt, KB, Kheiss Belt; NNB, Namaqua-Natal Belt; CFB, Cape-Fold Belt; CL, Colesburg Lineament and OT, Okwa Terrane.

to image the crust and upper mantle beneath the cratons and the adjacent Proterozoic provinces. Mantle structure has been imaged using both body wave and surface wave tomography (e.g. James *et al.* 2001; Fouch *et al.* 2004; Li & Burke 2006; Chevrot & Zhao 2007). However, due to the lack of regional seismicity and the lateral spacing limitations of the seismic array in southern Africa, it is difficult to image high-resolution seismic structures in the entire crust with either teleseismic body wave or surface wave tomography. As pointed out by James *et al.* (2001),  $P$ -wave velocity structure above 50 km cannot be obtained from teleseismic body wave tomography given the  $\sim 100$  km grid spacing of the array. Surface wave tomography can only produce velocity maps at periods longer than  $\sim 20$  s, which mainly constrains the upper mantle rather than the crust.

Aspects of crustal structure, including Moho depth, have been inferred from receiver function analysis in southern Africa. For example, Nguuri *et al.* (2001) showed that the crust beneath the undisturbed Archaean craton is typically rather thin ( $\sim 37$  km) and is characterized by a strong velocity contrast across a relatively sharp Moho. In contrast, the crust tends to be relatively thick ( $\sim 45$  km) and the Moho is complex beneath the post-Archaean terranes. The nature of the Archaean crust is clearly distinguished from the post-Archaean terranes. Seismic images of the crust and uppermost mantle would help further to decipher the formation and evolution of Archaean cratons.

Surface wave tomography based on cross-correlations of long-time sequences of ambient seismic noise provides a powerful new tool to image the velocity structures in the crust and uppermost mantle because empirical Green's function of surface waves between pairs of stations at periods as short as 6 s over large areas can be obtained. Applications of ambient noise surface wave tomogra-

phy both on continental (Yang *et al.* 2007; Bensen *et al.* 2007b) and regional scales (Shapiro *et al.* 2005; Kang & Shin 2006; Yao *et al.* 2006; Lin *et al.* 2007a,b; Villaseñor *et al.* 2007; Moschetti *et al.* 2007) have successfully produced group and phase velocity maps with velocity anomalies that are closely related to geological features, such as sedimentary thickness, crustal thickness and crustal velocities.

In this study, we perform cross-correlations of ambient noise data recorded at the stations of the SASE project. Rayleigh wave phase velocities between all station-pairs are measured at periods from 6 to 40 s from the cross-correlations. Surface wave tomography is conducted to generate phase velocity maps. We combine these phase velocity maps with maps at periods from 45 to 143 s derived from teleseismic two-plane wave tomography (Li & Burke 2006), to develop a high-resolution 3-D shear wave model of the crust and uppermost mantle beneath southern Africa.

## DATA PROCESSING

The SASE experiment operated from April 1997 until July 1999 and consisted of 82 broad-band seismic stations with roughly a 100 km station interval. The stations were deployed across southern Africa from the Cape Fold belt in the southwest to the Zimbabwe craton in the northeast (Fig. 1). Thirty-two stations continuously recorded data during the 2-yr experiment, and another 23 stations were moved to different locations after the first year. Three broad-band digital stations from the Global Seismic Network are also used in our analyses.

We use continuous vertical-component seismic data that were recorded over a period of 2-yr. The data processing procedure applied here is very similar to that described in detail by Bensen *et al.* (2007a). Using only the vertical component of ambient noise, however, implies that the cross-correlations we obtain contain only Rayleigh wave signals. We filter the data between 4 and 50 s period. Fig. 2 shows an example of a record-section of cross-correlations with respect to the common station SA39, which is near the centre of the SASE array (Fig. 1). Time series lengths range from one to two years in duration. Prominent signals are seen for both positive and negative correlation lags with an average move-out velocity of  $\sim 3$  km  $s^{-1}$ . The signals at positive and negative lags represent waves travelling in opposite directions between the stations; they sample

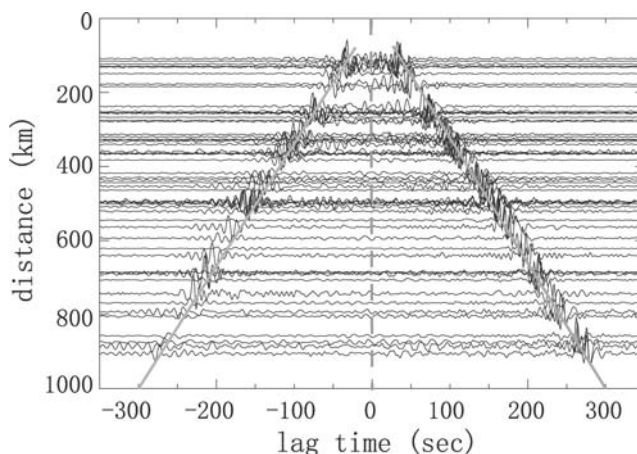


**Figure 2.** Broad-band (5–50 s period) record section of cross-correlations with the central station SA39 (see Fig. 1). Both positive and negative correlation lag times are shown. The two inclined grey lines mark a moveout velocity of 3 km  $s^{-1}$ .

the same media between a station-pair and are expected to travel with the same dispersion characteristics. To simplify data analysis and enhance the SNR, we separate each cross-correlation into positive and negative lag components and then add the two components to form a final cross-correlation, which we call the ‘symmetric component’. The following analysis is performed on the symmetric components exclusively.

Previous theoretical studies (e.g. Lobkis & Weaver 2001; Snieder 2004; Roux *et al.* 2005) and the observational study of Lin *et al.* (2007b) demonstrated that empirical Green’s functions between two stations can be obtained from the cross-correlation function by taking the negative of the time derivative except for a frequency-dependent amplitude correction. Thus, prior to phase velocity measurements, we perform negative time derivatives on all cross-correlations to obtain empirical Green’s functions.

To evaluate the quality of the cross-correlations quantitatively, we calculate the period-dependent signal-to-noise (SNR) for each interstation cross-correlation. SNR is defined as the ratio of the peak amplitude within a time window containing the surface wave signals to the root-mean-square of the noise trailing the signal arrival window. The signal window is determined using the arrival times of Rayleigh waves at the minimum and maximum periods of the chosen period band (5–50 s) predicted by the global 3-D shear velocity model of Shapiro & Ritzwoller (2002). The period dependence of the SNR is determined by applying a series of narrow bandpass filters centred on a grid of periods from 5 to 50 s. Fig. 3(a) shows an example of a symmetric component broad-band cross-correlation decomposed into five narrow bandpass filtered time series with the central periods indicated in the individual panels. Rayleigh wave signals show up clearly in each of these period bands. Fig. 3(b) (solid line) displays the corresponding SNR as a function of period. SNR in this example (and generally) is higher in the microseism band (5–20 s) than at longer periods (>20 s). The peak SNR is around 7 s here, near the centre of the secondary microseism band (5–10 s). In many such examples worldwide a second maximum in SNR appears at about 15 s period, but this peak is absent in this example.

Fig. 3(b) also presents the average interstation SNR taken over the entire SASE data set with the black bold line. Comparison of these values with those obtained in different regions of the world is difficult because they depend on path-length, time-series length, the local noise conditions, and also on the details of the filters applied

in computing the SNR values, which may differ between studies. SNR, however, in southern Africa is definitely higher than in Europe (Yang *et al.* 2007). It also appears to be higher than anywhere in the US, being most similar to the conditions in southern California (e.g. Bensen *et al.* 2007b), and is also similar to the ambient noise conditions in New Zealand (Lin *et al.* 2007a). This is presumably because the array is surrounded on three sides by relatively nearby coastlines where ambient noise is created and it is also a testament to the high quality siting, installation, and maintenance by the SASE team.

As discussed in the next section, SNR is one criterion used to select acceptable measurements. The high SNR conditions of the SASE array in southern Africa allow us to retain only high SNR cross-correlations for the dispersion measurements, which yields a more reliable data set.

## PHASE VELOCITY MEASUREMENT AND TOMOGRAPHY

Most ambient noise tomography that has been performed to date has concentrated on measuring the group velocity of surface waves (e.g. Shapiro *et al.* 2005; Moschetti *et al.* 2007; Villaseñor *et al.* 2007; Yang *et al.* 2007). Group velocity is measured from the arrival time of the peak of the amplitude envelope. Phase velocity is measured from the instantaneous phase, which is then converted to travel time. As argued by Bensen *et al.* (2007a) and Lin *et al.* (2007b), phase velocity measurements have three advantages over group velocity measurements. First, the uncertainty of the phase velocity measurement is much smaller than that of the group velocity measurement. Second, at the same period, phase velocity has a deeper sensitivity kernel and, therefore, constrains deeper velocity structures. Third, the dispersion relation for group velocity can be calculated from the dispersion relation for phase velocity, but the converse is not true.

We follow Lin *et al.* (2007b) and obtain phase velocity dispersion measurements for Rayleigh waves by automatic frequency-time analysis (FTAN). We resolve the phase ambiguity common to all phase velocity measurements by using the average phase velocities of Li & Burke (2006) in Southern Africa as the reference. Fig. 4 shows two examples of symmetric component cross correlations and the corresponding phase velocity dispersion curves. The path between stations SA02 and SA10 (red) lies mostly within the Proterozoic Namaqua-Natal belt, and the path between stations SA30

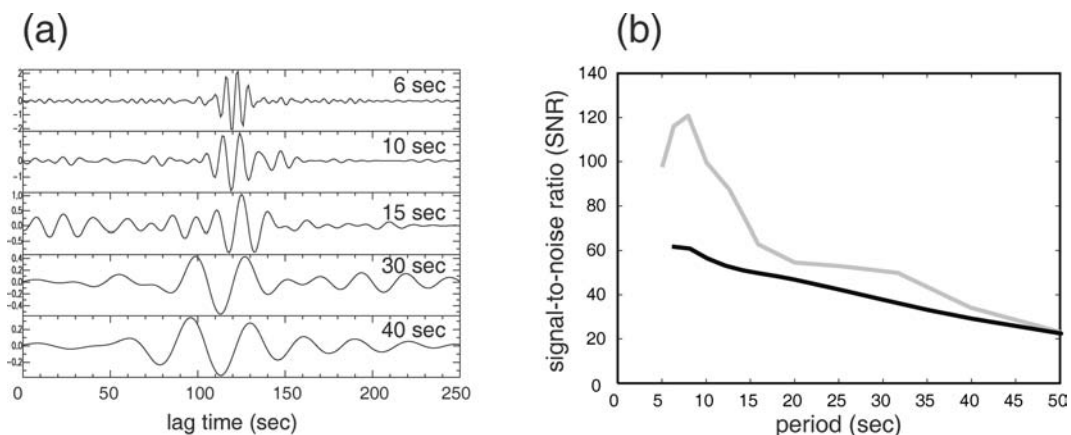


**Figure 3.** (a) Example of a symmetric-component cross-correlation using 12-months of data for stations SA39 and SA55, in which the various panels are narrow bandpass filtered with the indicated central period. (b) The grey line presents SNR values as a function of period for the cross-correlation shown in (a). The black line is SNR averaged over all of the cross-correlograms from the SASE array.

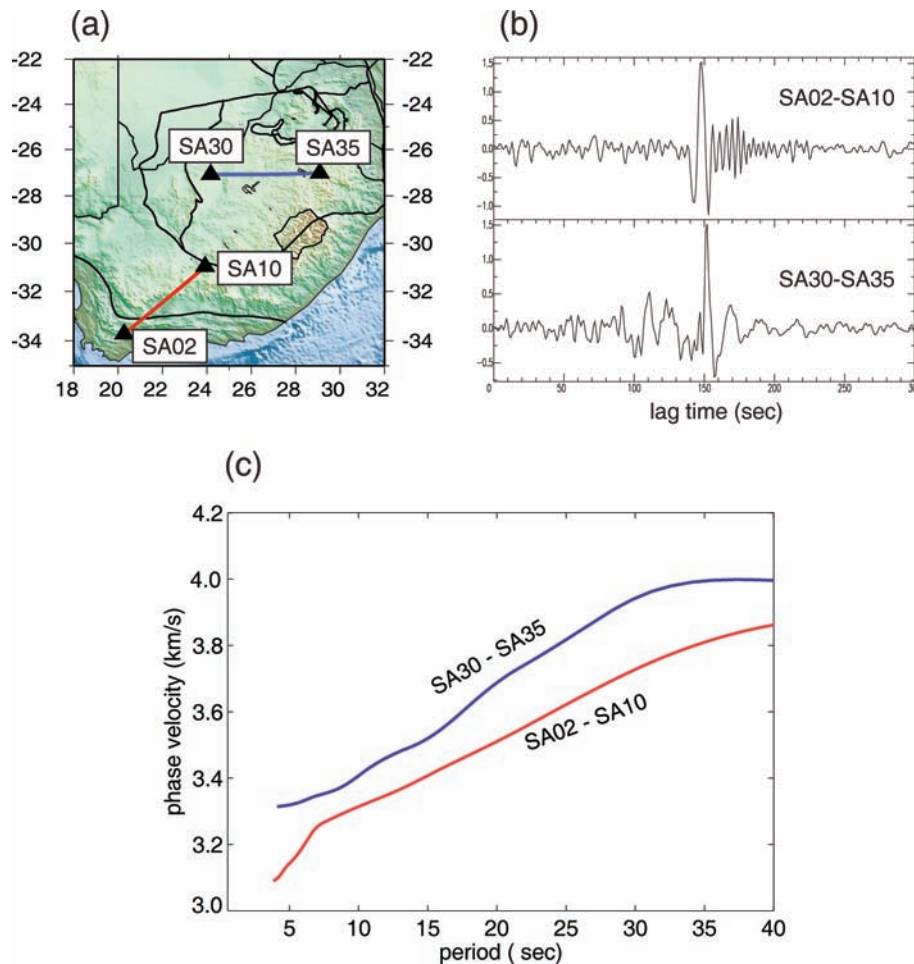


**Figure 4.** (a) Ray paths between stations SA02 and SA10 (red) and between stations SA30 and SA35 (blue). (b) 5–50 s bandpass filtered symmetric cross-correlations for station pairs SA02–SA10 and SA30–SA35. (c) The measured Rayleigh wave dispersion curves based on the symmetric cross-correlations shown in (b). The red curve is for the station pair SA02–SA10 and the blue curve for the station pair SA30–SA35.

and SA35 (blue) is within the Archaean Kaapvaal craton. Phase velocities in the Kaapvaal craton are significantly higher than in the Namaqua-Natal belt, which is probably the result of higher crustal velocities and a thinner crust (Nguuri *et al.* 2001) in the Kaapvaal craton than in the Namaqua-Natal belt. The dispersion curve in the cratonic region becomes relatively flat at periods longer than  $\sim 30$  s because Rayleigh wave phase velocity is most sensitive to the crust at short periods ( $< 30$  s) and most sensitive to the upper mantle at longer periods ( $> 30$  s) given the  $\sim 35$ –40 km crustal thickness in the Kaapvaal craton (Nguuri *et al.* 2001). This flattening of the phase velocity curve is not observed for the dispersion curve in the Namaqua-Natal belt, where the crust is thicker,  $> 45$  km (Nguuri *et al.* 2001). In this region of thick crust, phase velocities at periods shorter than 40 s are mostly sensitive to crustal velocities.

The automated measurement procedure is followed by the application of three criteria to select the reliable measurements for tomography. First, the distance between two stations must be greater than three wavelengths to ensure that reliable dispersion measurements can be obtained. Thus, each dispersion curve is retained only up to a period equal to one-third of the observed travel time. Second, the SNR must be higher than 20 at an individual period for the measurement at that period to be accepted. As shown by Bensen *et al.* (2007a), SNR is in many cases a good indicator of the reliability

of the dispersion measurements from cross-correlations and provides a useful proxy for uncertainties. Bensen *et al.* (2007a) advocate using the seasonal variability of the dispersion measurements as measurement uncertainties that then act as an additional basis for selection. The variable time-series lengths of the SASE experiment make this somewhat difficult, so we rely exclusively on SNR as a proxy for measurement uncertainty. The SNR threshold of 20 is quite conservative and helps to ensure that the chosen measurements are reliable. Third, we require that the measurements agree with one another across the data set. This condition is tested during tomography. Measurements that can be fit well by a smoothed tomographic map are considered coherent.

One of main concerns in ambient noise tomography is that whether accurate empirical Green's functions can be retrieved from cross-correlations of ambient noise and whether the observations can be used meaningfully to obtain dispersion measurements when the distribution of ambient noise is not homogenous. To address this question, Yang & Ritzwoller (2008) have performed a series of synthetic experiments with inhomogeneous noise energy distributions. Their synthetic experiments show that if ambient noise exists over a broad azimuthal range even at relatively low levels, accurate empirical Green's functions will emerge from long time series of the ambient noise even when the distribution is far from azimuthally homogenous.

Our data selection criteria result in 2100–2400 of the 3570 original interstation phase speed measurements being chosen for tomography at 6–20 s period. This number reduces with period so that at 30 s there are about 1300 measurements chosen for tomography and at 40 s there are about 750. The number of measurements continues to drop with period above 40 s, rendering tomography impossible at longer periods. The reduction in number of measurements largely results from the three-wavelength selection criterion.

The Rayleigh wave phase velocity measurements are used to invert for phase velocity maps on an  $1^\circ \times 1^\circ$  spatial grid across southern Africa using the tomographic method of Barmin *et al.* (2001). This method is based on minimizing a penalty functional composed of a linear combination of data misfit, model smoothness and the perturbation to a reference model for isotropic wave speed. The choice of the damping parameters is subjective, but we perform a series of tests using different combinations of parameters to determine acceptable values by considering data misfit, model resolution, and model norm. More details about this method can be found in Yang *et al.* (2007). The tomographic method is based on ray theory with great-circle paths and Gaussian shaped lateral sensitivity kernels. Detailed finite-frequency effects at this period and interstation distance range are smaller than variations in the maps caused by the arbitrariness inherent in damping and smoothing. Off-great circle propagation is a greater concern at the short period end of this study, but the lateral inhomogeneities in this region are sufficiently smooth with low amplitudes to mitigate these effects. Thus, the ray theoretic approach we take is sufficient for the purposes of ambient noise tomography at the periods analysed in this region.

Resolution is estimated also by using the method described by Barmin *et al.* (2001) with modifications presented by Levshin *et al.* (2005). Each row of the resolution matrix is a resolution surface (or kernel). We summarize the information in the resolution surface at each spatial node by fitting a 2-D symmetric spatial Gaussian function to the surface at each node:  $A \exp(-\frac{|r|^2}{2\gamma^2})$ . The spatssial resolution at each node is defined as twice the standard deviation of this Gaussian function:  $2\gamma$ .

Examples of path coverage and resolution are shown in Fig. 5 for the 8, 16 and 30 s measurements. At the longer periods, there is a reduction in path density and resolution due to the decrease in the number of measurements, which is caused by the three-wavelength criterion and the general reduction in SNR above 20 s period (Fig. 3). The resolution of surface wave tomography depends primarily on the azimuthal distribution and density of paths, which are best in the centre of the study region but deteriorate near its edges. As a result, resolution is estimated to be about 100 km across most of the study region, but degrades toward the periphery of the maps.

## PHASE VELOCITY MAPS

Phase velocity tomography is performed in two steps. The first, preliminary, step generates overly smoothed maps at each period in order to identify and reject bad measurements. This comprises the third selection criterion mentioned in the previous section. The overly smoothed maps fit most data well as the example misfit histograms for the 10, 16 and 30 s data sets show in Fig. 6. We discard phase velocity measurements with travel time residuals larger than 3 s, which is about three times the RMS value of the travel time residuals at most periods. The second step of tomography is the construction of the final maps. Maps are constructed on an  $1^\circ \times 1^\circ$

spatial grid across southern Africa and are defined relative to the average velocity across the study region.

The results of phase velocity tomography at 6, 16, 25 and 40 s periods are shown in Fig. 7. The features of the maps vary gradually with period due to the overlap of the Rayleigh wave depth-sensitivity kernels. Most of the observed velocity anomalies are correlated with known geological units, which we discuss further below. The depth of maximum phase velocity sensitivity of Rayleigh waves is about one-third of a wavelength. At the short-period end of this study (6–10 s), phase velocities are dominantly sensitive to shear velocities in the upper crust. Because the seismic velocities of sediments are very low, short-period low velocity anomalies are a good indicator of sedimentary basins. At the long period end of the ambient noise dispersion measurements (25–40 s), Rayleigh waves are primarily sensitive to crustal thickness and the shear velocities in the lower crust and uppermost mantle. Due to the large velocity contrasts across the Moho, the phase velocities between 25 and 40 s period should vary approximately inversely with crustal thickness, with high velocities in regions with thin crust and low velocities in regions with thick crust.

The 6 and 16 s phase velocity map shown in Figs 7(a) and (b) exhibits low velocities in the Proterozoic Namaqua-Natal belt and the Okwa terrane of eastern Botswana and high velocities in the Archaean Zimbabwe craton, the Limpopo mobile belt, and the western part of the Kaapvaal craton. At the period of 6 s, low velocities appear in the eastern part of the Kaapvaal craton, which could be related to the ancient sedimentary basin there that resulted from extensional tectonics in the late Archaean (de Wit *et al.* 1992). Overall, in this period range the velocity anomalies are much smaller than those obtained in non-cratonic regions elsewhere in the world, such as California (e.g. Shapiro *et al.* 2005; Lin *et al.* 2007b; Moschetti *et al.* 2007), across much of the US (Bensen *et al.* 2007b), and Europe (Yang *et al.* 2007).

At periods from 25 to 40 s (Figs 7c and d), phase velocities become increasingly sensitive to crustal thickness. The estimated maps exhibit high velocities in the undisturbed Kaapvaal and Zimbabwe cratons. The lowest velocity anomalies are imaged in the Namaqua-Natal belt and relative low velocities also appear in the Okwa terrane, the Bushveld complex, and the Limpopo orogenic belt. As will be seen in the next section, phase velocities at periods of 25 and 40 s are strikingly correlated with crustal thicknesses estimated with receiver functions by Nguuri *et al.* (2001). High phase velocities are correlated with thin crust and low velocities with thick crust.

Dispersion maps at periods longer than 40 s cannot be obtained from ambient noise tomography using the SASE array data alone. This is due to that the three-wavelength criterion limits the number of dispersion measurements at longer periods. Longer period dispersion characteristics of surface waves can be measured from teleseismic events when they propagate over a regional array of seismometers. Thus, in this study, we constrain upper mantle structures using dispersion measurements from teleseismic Rayleigh waves at periods from 45 to 143 s taken directly from Li & Burke (2006).

Li & Burke (2006) obtained phase velocities at periods from 20 to 167 s in southern African using more than 200 teleseismic events recorded at the same SASE stations at which we perform ambient noise tomography. They adopted the ‘two-plane wave’ method, which interprets the variation in amplitude and phase of teleseismic surface waves in terms of phase velocity variations within the array and models the incoming teleseismic wavefield using the sum of two plane waves, each with initially unknown amplitude, initial phase, and propagation direction (Forsyth *et al.* 1998; Forsyth & Li 2005). This two-plane wave representation has been applied

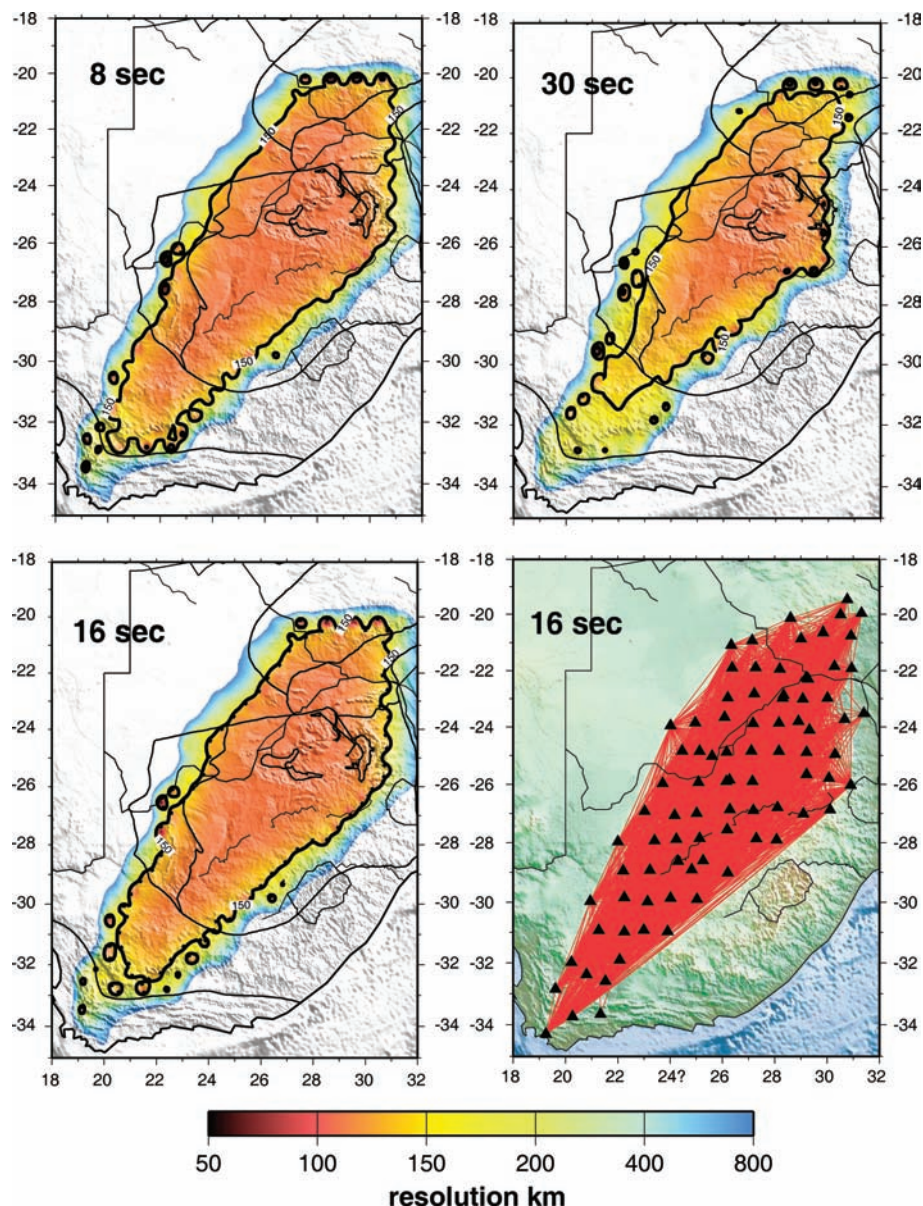


**Figure 5.** Resolution estimates at 8, 16 and 30 s period with path coverage at 16 s shown at lower right. Resolution is presented in units of kilometre, and is defined as twice the standard deviation of a 2-D Gaussian fit to the resolution surface at each model node. The contour of 150 km resolution is shown with a bold black line.

successfully to regional arrays in both continental and oceanic areas to obtain phase velocities and information about azimuthal anisotropy (Li *et al.* 2003; Weeraratne *et al.* 2007; Yang & Forsyth 2006a,b). Li & Burke (2006) applied two-plane-wave tomography in southern Africa using a Cartesian geometry and Gaussian-shaped lateral sensitivity kernels. Application of the two plane-wave method of Yang & Forsyth (2006b), which includes finite-frequency kernels in a spherical geometry, to the same data set yields very similar results. However, the size of the area of study is near the limit of the two-plane wave assumption in either Cartesian or spherical coordinates. Partitioning the region into overlapping subregions yields very similar results, which establishes that two-plane waves are sufficient.

Ambient noise tomography and the teleseismic two-plane wave method have complementary strengths and weaknesses. Ambient

noise tomography provides stable information about surface wave dispersion at periods ranging from 5 to 40 s. This band does not provide information about the upper mantle deeper than about 60 km, however. The two-plane wave method provides information only at periods longer than 20 s because of scattering and attenuation that occurs along the path from the teleseismic source. Both methods can produce similar resolution, estimated to be at about the interstation spacing of SASE Array (i.e.  $\sim 100$ – $150$  km) at periods below about 40 s (Fig. 5). Resolution degrades at longer periods. In the frequency band of overlap, the methods produce consistent phase velocity maps. Examples of phase velocity maps at 30 s period are shown in Fig. 8. Agreement is best in the middle of the array where data coverage is highest for both methods. Differences are most pronounced near the fringes of the array where resolution is lower.

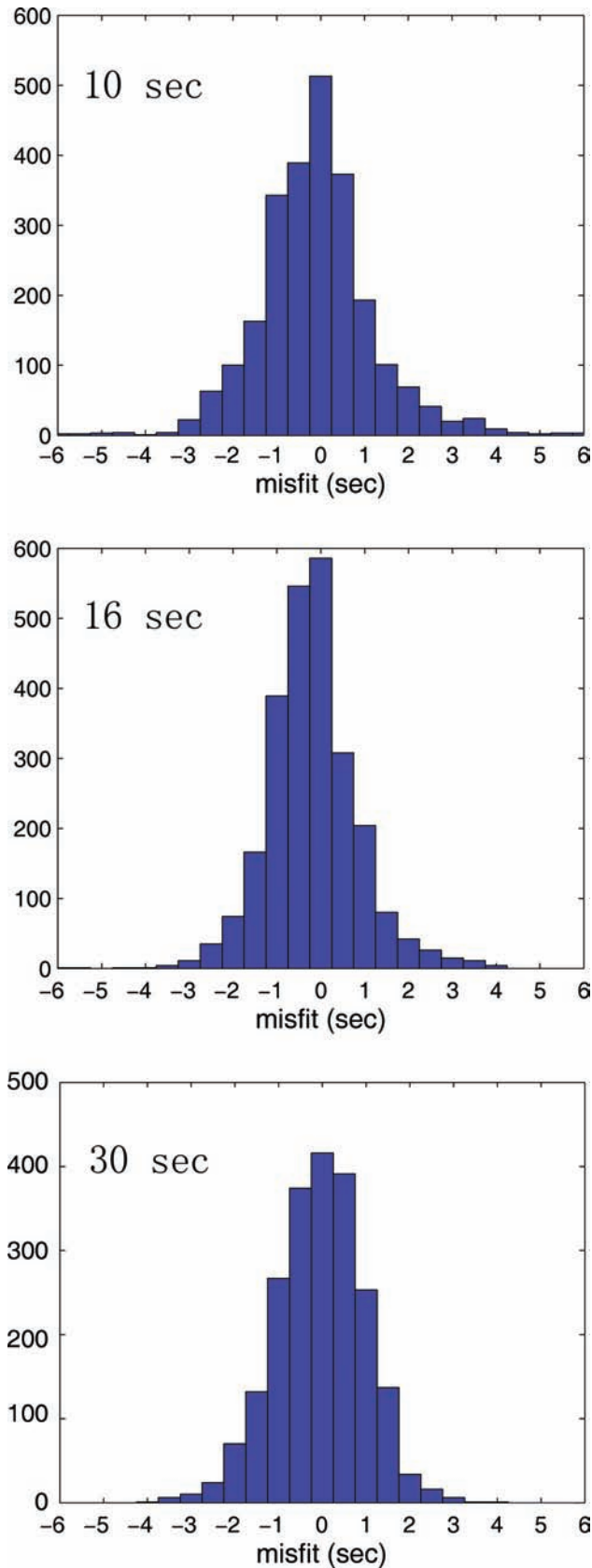


**Figure 6.** Histograms of tomographic misfits at 10, 16 and 30 s period. Misfits are calculated from the differences between observations and predictions for the oversmoothed tomographic maps. Positive values mean observations are larger than predictions.

## SHEAR WAVE VELOCITY STRUCTURE

More detailed interpretation of the observed phase velocity anomalies requires inversion for the  $V_s$  structure of the crust and uppermost mantle. The phase velocity maps from ambient noise tomography at periods from 6 to 40 s provide unprecedented constraints on crustal thickness and shear wave velocities in the crust and uppermost mantle beneath southern Africa. At periods from 45 to 143 s we use the phase velocity maps of Li & Burke (2006). Inversions using only the ambient noise dispersion maps show that crustal velocities, crustal thicknesses, and uppermost mantle structures to a depth of about 60 km are relatively unaffected by the longer period maps. The maps of Li & Burke (2006), therefore, predominantly affect the 3-D model in the mantle below 60 km. Our focus, therefore, will be on the model of the crust and uppermost mantle to 60 km depth, although images to 100 km are also shown here. Model parameters in this inversion are shear wave velocities in 10 layers from the Earth's surface to 200 km depth with 10–30 km layer thicknesses. The thickness of each layer is kept fixed except that the two layers right above and below Moho are allowed to vary in order to accommodate the variation of Moho topography.

Rayleigh wave phase velocities primarily depend on  $S$ - and  $P$ -wave velocities, less on density. Thus in the inversion, we fix the densities using the AK135 density model. Because the sensitivity of surface waves to  $P$ -wave velocity in the upper mantle is negligible compared to that of  $S$ -wave velocity and the choice of different Poisson's ratios in the inversion has no significant effect on  $S$ -wave velocity in the upper mantle, we only estimate  $S$ -wave velocity by scaling  $P$ - to  $S$ -wave velocity assuming the materials of upper mantle are Poisson solids. The sensitivity to  $P$ -wave velocity becomes strong in the crust, especially for surface waves at periods shorter than 20 s, which are mainly sensitive to crustal structures. Therefore, we use Poisson's ratios from a receiver function study by Nair *et al.* (2006) as constraints in the crust when we invert for  $S$ -wave velocity. In fact, because only Rayleigh waves are used in the inversion, the primary sensitivity is to  $V_{sv}$ , which may vary from  $V_s$  by several per cent in the uppermost mantle due to radial anisotropy and in some instances may also vary from  $V_s$  in the crust (e.g. Shapiro *et al.* 2004). Because we did not study Love waves across southern Africa, we have no  $V_{sh}$  information, so can say nothing yet about the strength or distribution of radial anisotropy in the upper mantle. Hereafter, although we will refer to the model as a  $V_s$ -model, it is in fact  $V_{sv}$ .

The relation between shear wave speeds and phase velocities is non-linear. We linearize the relation and iterate until convergence using Saito's algorithm (Saito 1988) to compute the synthetic phase velocities and partial derivatives with respect to changes in  $P$ - and  $S$ -wave speeds.  $P$ -wave velocities are tied to  $S$ -wave velocities using a constant Poisson's ratio in the upper mantle and a laterally varying Poisson's ratio model from Nair *et al.* (2006) in the crust. Because of the nonlinearity and also due to the limitations of surface wave vertical resolution, the model parameters are weakly damped by assigning prior standard deviations of  $0.05 \text{ km s}^{-1}$  to the diagonal terms of the model covariance matrix and are also smoothed by adding terms equal to 0.3 to the first off-diagonal. The value of  $0.05 \text{ km s}^{-1}$  for the prior parameter errors was determined after several experiments with different values from 0.002 to  $0.15 \text{ km s}^{-1}$ . The aim is to produce a model that is vertically smooth but also is free to vary significantly from the starting model.

In order to obtain an appropriate reference or starting model for the study region, we first perform an inversion using the average phase velocities for the entire region with AK135 as the starting

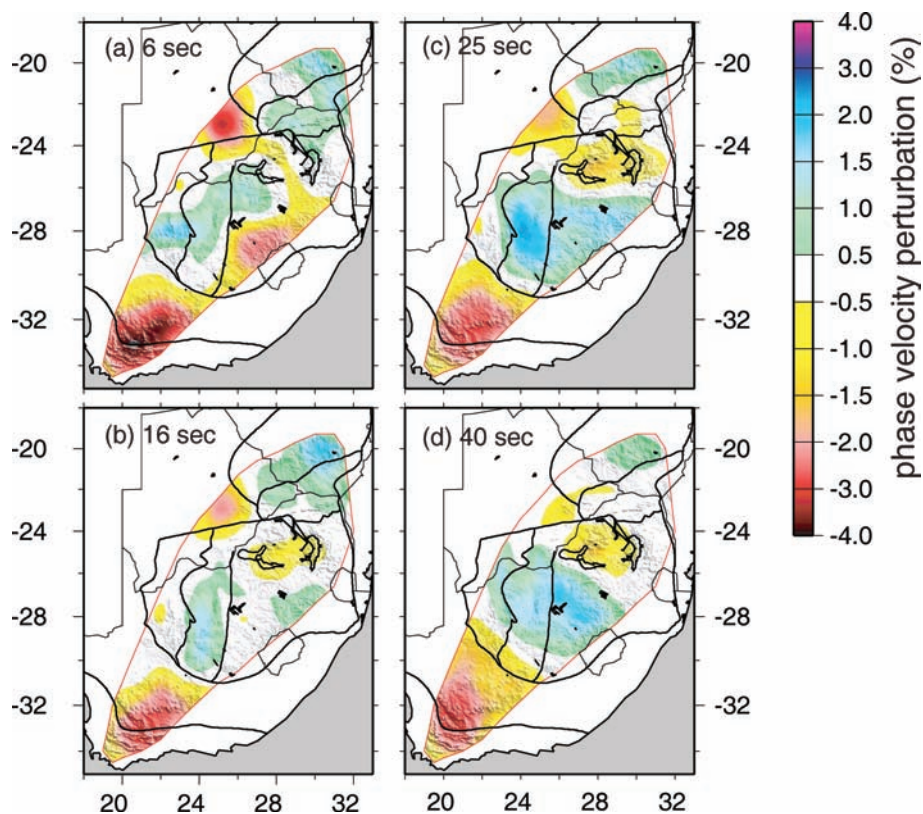


**Figure 7.** Estimated phase velocity maps at 6, 16, 25 and 40 s periods. Maps are presented as the perturbation to the average value (Fig. 8) across the map in per cent. Only the station-covered area is shown within the red contour. This same clipping contour is used in Figs 8, 10, 11 and 13.

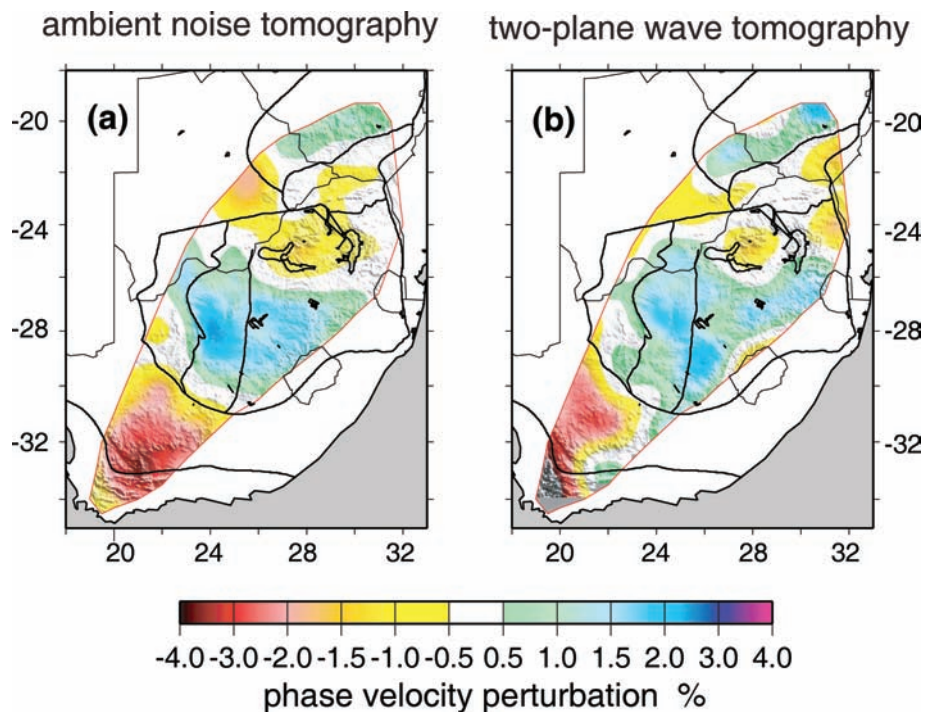


**Figure 8.** Phase velocity maps at 30 s period based on ambient noise tomography (left-hand side) and teleseismic two-plane wave tomography (right-hand side). Maps are presented as a perturbation to the average phase velocity at 30 s period (Fig. 9).

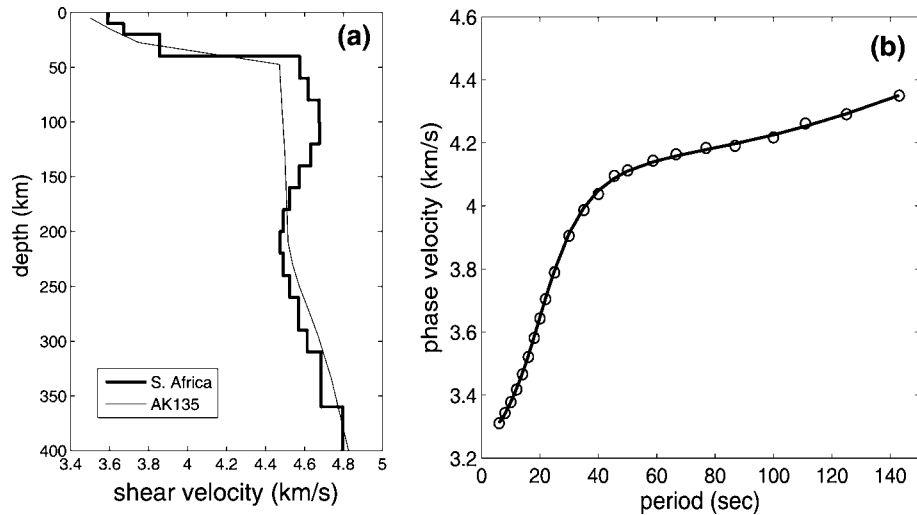


**Figure 9.** (a) The average (1-D) shear wave velocity structure inferred for southern Africa (bold line). The AK135 model (thin line) (Kennett *et al.* 1995) is plotted for comparison. (b) Average phase velocities across southern Africa (circles) and predictions from the 1-D model (bold line). Observations from 6 to 40 s are taken from ambient noise tomography and from 45 to 143 s period from teleseismic two-plane wave tomography (Li & Burke, 2006).

model, but with the lower crust extended to a depth of 39 km which is near the average from the receiver function study of Nguuri *et al.* (2001). We also have performed the inversion with different initial models and have found that their effect on the average  $V_s$  velocity is small. The 1-D reference model is plotted in Fig. 9(a) and the associated phase velocities that are averaged over the study region are shown in Fig. 9(b). This 1-D  $V_s$  model is almost the same as that of Li & Burke (2006) because the same phase velocities at periods longer than 40 s are used and the average phase velocities in the overlapping period band from 20 to 40 s are also quite similar. As Li & Burke (2006) show, on average across the region of study, there is a fast mantle lid (compared with AK135, for example) to a depth of  $\sim 180$  km with a shear wave velocity of  $\sim 4.67$  km s $^{-1}$  and a weak low-velocity zone beneath the mantle lid to a depth of  $\sim 260$  km. Because  $V_{sh} > V_{sv}$  on average in the uppermost mantle, correction of our  $V_{sv}$  model to  $V_s$  for radial anisotropy would probably make the model faster. Thus, the difference be-

tween the model and AK135 in the upper mantle is probably a lower bound.

We applied the same method used in the average 1-D inversion at each spatial grid point to obtain the 3-D shear wave structure in southern Africa. Results of the inversion are shown in Figs 10 and 11. Three-dimensional variations of the shear wave structure in the upper mantle deeper than 100 km beneath southern Africa are already discussed in another paper (Li & Burke 2006).

Fig. 10 presents the estimates of crustal thickness. Fig. 10(a) is the interpolated model of Nair *et al.* (2006) obtained from receiver functions. Fig. 10(b) shows the crustal thickness obtained from the ambient noise phase velocity maps alone (6–40 s period). Crustal thickness from the ambient noise study varies more smoothly than that from receiver functions due to the different lateral resolution between surface and body wave. Both maps show similar features with relatively thin crust in the Kaapvaal and Zimbabwe cratons and thick crust in the mobile belts. There are, however, some

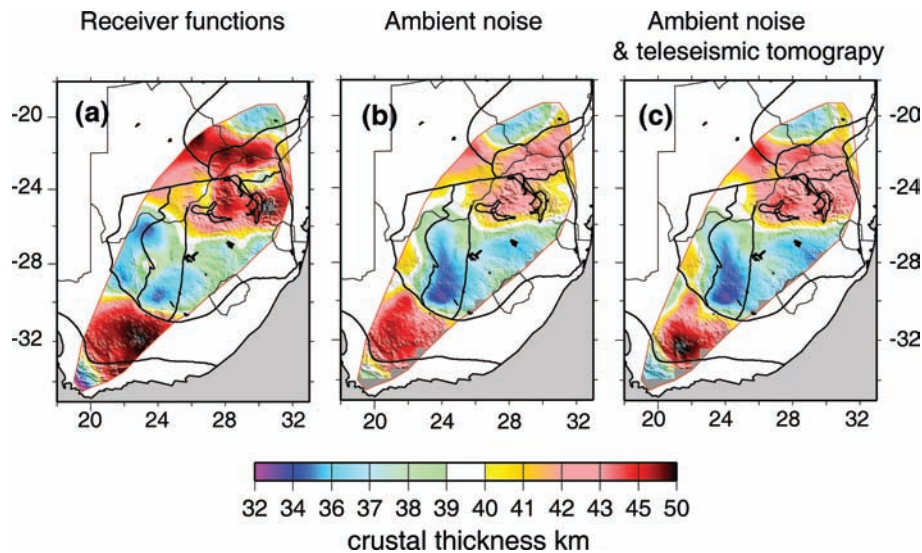


**Figure 10.** (a) Crustal thickness inferred from receiver functions by Nair *et al.* (2006). (b) Crustal thickness inferred from ambient noise data alone (i.e. phase velocities from 6 to 40 s). (c) Crustal thickness inferred from ambient noise and teleseismic two-plane wave tomography (i.e. phase velocities from 6 to 143 s).

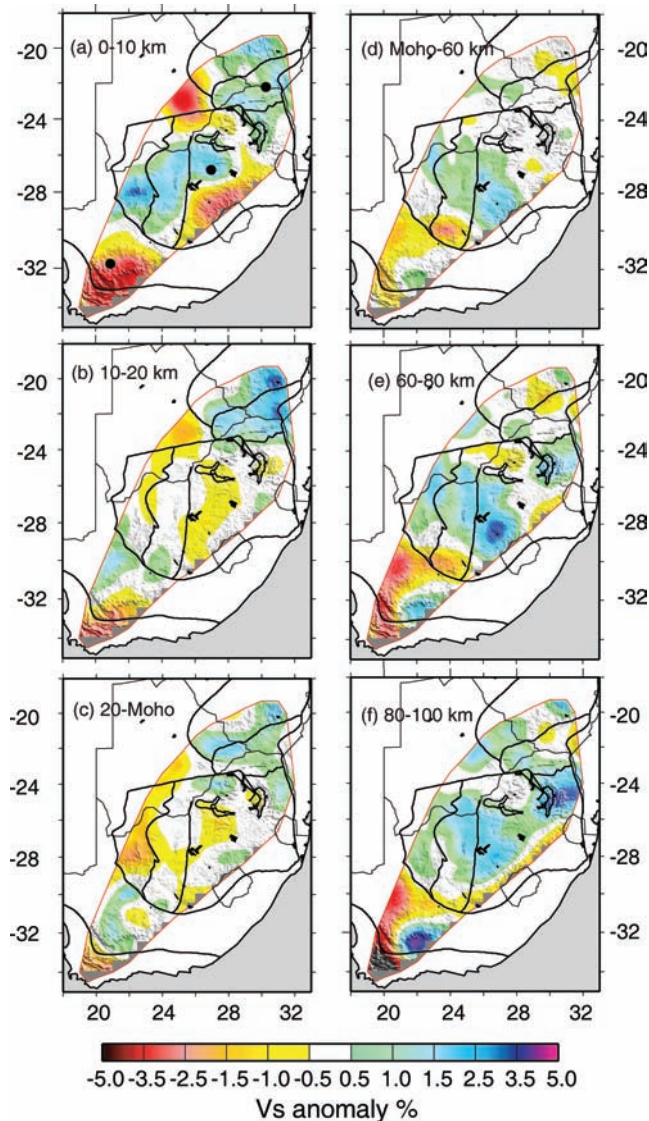


**Figure 11.** Maps of shear wave velocity anomalies in six layers extending from the upper crust to a depth of 100 km. The velocity anomalies are defined relative to the 1-D reference model shown in Fig. 9(a) (bold line). Black circles in (a) marks the sites of the three vertical profiles in Fig. 14.

discrepancies between the crustal thickness from the receiver function and that from surface wave tomography in some regions where the crustal thickness from the receiver functions is not constrained very well due to the inability to obtain a reliable  $V_p/V_s$  ratio (Nair *et al.* 2006). This result from the ambient noise phase velocities is insensitive to the starting model, given the relatively low amplitude of Moho topography in southern Africa. For example, estimated crustal thickness is essentially identical starting either from a homogeneous crustal depth of 39 km or from the Nair model. Fig. 10(c) shows crustal thickness using both the ambient noise and two-plane wave dispersion maps (6–143 s period). With the exception of the very thick crust that emerges in the southeastern Namaqua-Natal Belt, the results are very similar. Thus, the crustal thickness estimates depend exclusively on the ambient noise dispersion measurements.

Fig. 11 presents shear wave velocity perturbation maps with respect to the 1-D  $V_s$  model (Fig. 9) in six layers, three in the crust and three in the uppermost mantle. Although the upper crust (0–10 km) has larger amplitude velocity anomalies than the mid-

dle crust, the variation of upper crustal velocities is small compared to many regions in the world (e.g. California, Yang & Forsyth 2006b). This is expected, due to the great age of the sediments in the region and the interpenetration of the sedimentary basins by volcanics. In the upper crust, relative high shear wave velocities of  $3.62\text{--}3.70\text{ km s}^{-1}$  are imaged in the central and western Kaapvaal craton, the Limpopo belt, and the Zimbabwe craton. Low velocity anomalies appear in younger terrains bounded by the Kaapvaal and Zimbabwe cratons, such as the Namaqua-Natal orogenic belt, the Cape-Fold belt, and the Okwa province. A slow shallow crust is also found in the Witwatersrand basin in the central and eastern Kaapvaal craton. The slow anomalies are largely attributed to relatively thick sedimentary layers in the Namaqua-Natal belt and the Witwatersrand basin, as imaged in seismic reflection and refraction profiles (Green & Durrheim 1990; Durrheim & Green 1992; De Wit & Tinker 2004). A more mafic Archean upper crust (Durrheim & Mooney 1994) may also contribute to the higher velocities observed in the uppermost crust beneath parts of the Kaapvaal and Zimbabwe cratons.

With the exception of high velocities beneath the Limpopo belt and the Zimbabwe craton, the middle and lower crustal layers from 10 km to the Moho in Fig. 11 has only small amplitude anomalies. These anomalies are approximately anticorrelated with those in the top crustal layer, particularly beneath the Kaapvaal craton. This anticorrelation is robust. For example, if we hold the upper layer constant and homogeneous in the inversion, approximately the same middle and lower crustal model results. The middle and lower crust is, on average, slow in the Kaapvaal craton and relatively fast in the Limpopo belt and the Namaqua-Natal belt. This pattern generally agrees with the global observation that Archean crust lacks the basal high-velocity layer that is present in the Proterozoic crust (Durrheim & Mooney 1991, 1994). The slowest lower crust is found in the western margin of the Kaapvaal shield at the Kheiss thrust belt, which may be associated with the extension around 1.9 Ga at this Atlantic-type margin, as has been imaged by seismic reflection profiles (Tinker *et al.* 2002). The slow lower crust in the Bushveld Complex is consistent with a model from receiver function inversion (Webb *et al.* 2004).

$V_p/V_s$  ratios in crustal rocks are sensitive to rock compositions and generally increase with higher mafic contents (Holbrook *et al.* 1992; Zandt & Ammon 1995). Nair *et al.* (2006) found that  $V_p/V_s$  ratios in the Kaapvaal craton are on average less than 1.73 except in the northern part of the craton including the western Bushveld Complex. A  $V_p/V_s$  ratio of 1.8 was also reported by Durrheim & Green (1992) in northern Kaapvaal based on seismic refraction modeling, although it was interpreted differently as the presence of hydrated rocks. High and low shear wave velocity in the lower crust of the Kaapvaal craton roughly correlates with high and low  $V_p/V_s$  ratios (Nair *et al.* 2006), respectively. There is some discrepancy between our shear wave model and the  $V_p/V_s$  ratio distribution from Nair *et al.* (2006). For example, shear wave velocity in the lower crust is low in the Bushveld in our model while  $V_p/V_s$  ratio there is high (Nair *et al.* 2006). This could be due to the  $V_p/V_s$  ratio from receiver function being an average value for the whole crust, not for the lower crust only. However, upper and lower crustal layers may have different properties as revealed in our 3-D shear wave model.

The uppermost mantle from the Moho to 100 km depth beneath the entire study region is fast compared with AK135. There is, however, considerable geographical variability. The uppermost mantle to 60 km depth is fast beneath much of the Kaapvaal craton and is slow in the Namaqua-Natal, the Limpopo, and the Kheiss belts and their vicinities (Fig. 11d). This observation agrees with other

body and surface wave models in southern Africa (e.g. James *et al.* 2001; Fouch *et al.* 2004; Li & Burke 2006). The fast Kaapvaal cratonic lithosphere has been attributed to high Mg content and cold temperature (Jordan 1979, 1988), which together make the lithosphere mechanically strong. Relative low velocities in the Bushveld Complex may reflect high iron content associated with the intraplate intrusion at 2.05 Ga. High velocities in the central Kaapvaal Craton extend at least to a depth of 100 km. In contrast, the Zimbabwe craton is relatively slow in the uppermost mantle. Li & Burke (2006) and Chevrot & Zhao (2007) have also observed these differences in the mantle lithosphere beneath the Kaapvaal and Zimbabwe cratons.

The upper mantle layers deeper than 100 km are not shown here as they are very similar to the model by Li & Burke (2006), who presented a shear wave model from 50 to 410 km depth and discussed the cratonic lithosphere thickness and low velocity layer at 160–260 km.

### MONTE CARLO RESAMPLING AND UNCERTAINTY ESTIMATION

One particular concern in the  $S$ -wave velocity inversion of Rayleigh wave phase velocity dispersion measurements is the trade-off between crustal thickness and velocities of the lower crust and uppermost mantle. In order to estimate the uncertainties of  $S$ -wave velocity and crustal thickness and quantify the confidence level of the resulting  $V_s$  model in the preceding section, we perform a Monte Carlo resampling. The Monte Carlo resampling performs a random walk through model space to create an ensemble of acceptable shear velocity models that fit the dispersion curves within permitted uncertainties. In model parametrization, we divide the crust into three layers as we do in the preceding linearized inversion but parametrize velocities of upper mantle at depths above 250 km with five B-spline functions for the purpose of speeding computation and smoothing  $S$ -wave velocity. We use the result of the preceding linearized inversion as an initial model and define the allowed range of models based on this initial model. The velocities in the crust and upper mantle are allowed to vary within a  $\pm 5$  per cent range of the initial model. The thicknesses of the upper and middle crustal layers are fixed but the thickness of the lower crust is allowed to vary with

the constraint that the thickness of the whole crust must be within a  $\pm 5$  km range from the initial model. Rayleigh wave phase velocity dispersion curves are computed for each model using the code of Herrmann (1987). If the predicted dispersion curves match the measured results at an acceptable level, the model is retained. An acceptable model is defined as one having an average dispersion misfit at the level similar to the average data misfit in phase velocity tomography, which is about  $0.025 \text{ km s}^{-1}$ . More details about the Monte Carlo resampling can be found at Shapiro & Ritzwoller (2002) and Bensen *et al.* (2008).

An example of the Monte Carlo resampling is plotted in Fig. 12 for a point in the Kaapvaal Craton marked by the black dot in Fig. 11(a). One hundred  $V_s$  models (grey lines) with acceptable fit to the phase velocity dispersion measurements are created. The model ensemble in this example displays strong variability over different depths while all have similar variability in the resulting dispersion curves. Thus, the goodness of fit for a computed dispersion curve is not necessarily a clear indicator of a robust model. The average of the resulting ensemble of acceptable models is taken as the expected value (the bold black line). The standard deviation ( $SD$ ) of the ensemble provides the estimates of uncertainties of the shear velocities and crustal thickness.

Assembling all the results of Monte Carlo resampling performed for each geographic point on a  $0.5^\circ \times 0.5^\circ$  grid, we generate a 3-D  $V_s$  model and relevant uncertainty estimates. The 3-D velocity model is very similar to that determined through the linearized inversion (Fig. 11). Thus, we do not replot the  $V_s$  model here. Uncertainties of crustal thickness and shear velocities for the three crustal layers and two layers of upper mantle are plotted in Fig. 13. The average  $SD$  of crustal thickness is 2.6 km and the average  $SD$  of shear velocities at the upper, middle and lower crust are  $21.4$ ,  $37.2$  and  $58 \text{ m s}^{-1}$  (0.6, 1 and 1.5 per cent), respectively. In the upper mantle, the average  $SD$  at the depth range between the Moho to 60 km is  $56.6 \text{ m s}^{-1}$  (1.2 per cent). Beneath 60 km,  $SD$  is  $\sim 40 \text{ m s}^{-1}$  (0.8 per cent) nearly uniform to 250 km. The  $SD$  of shear velocity in the lower crust and uppermost mantle is larger compared to that at other depths, which is due to the trade-off between crustal thickness and shear velocities at depths just above and below the Moho. Throughout the depth range reported in this study (Fig. 11),  $SD$  is less than shear velocity anomalies with a typical value  $\sim 100 \text{ m s}^{-1}$  ( $\sim 2.5$  per cent) as shown in Fig. 11, indicating that the model is reliable.

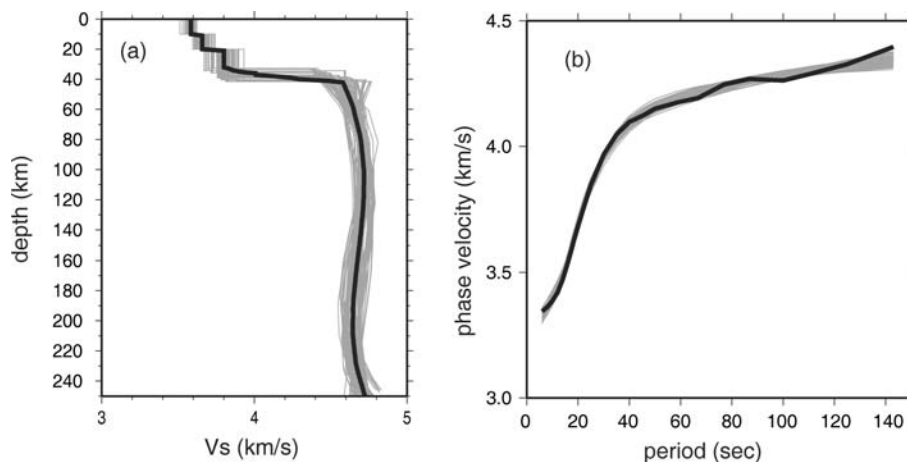


**Figure 12.** An example of the Monte Carlo resampling for a point marked by the black dot in the Kaapvaal craton in Fig. 11(a). (a) The resulting ensemble of acceptable  $V_s$  models (grey line) and the average of the ensemble (bold black line). (b) Grey lines are predicted dispersion curves from the ensemble of  $V_s$  models shown in (a). The bold black line is the observed dispersion curve.

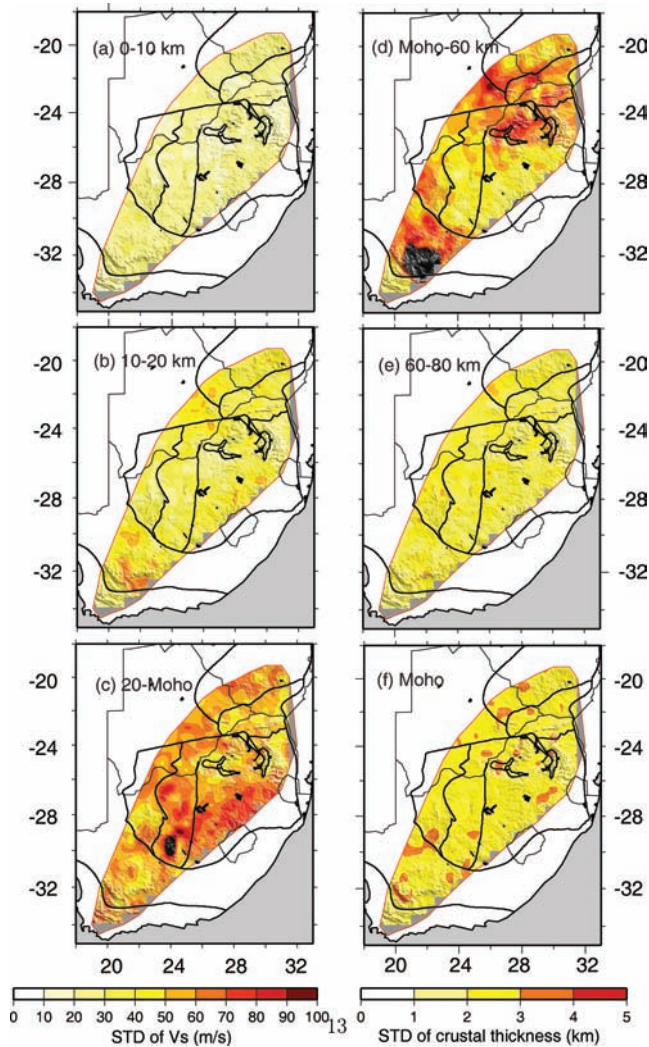


**Figure 13.** Maps of standard deviations ( $SD$ ) of shear wave velocity (a–e) in five layers extending from the upper crust to a depth of 80 km and crustal thickness (f).

## DISCUSSION AND CONCLUSIONS

Ambient noise tomography for Rayleigh wave phase velocity maps at periods from 6 to 40 s was performed for the first time using data from the SASE array in southern Africa. These observations were combined with phase velocity maps at periods from 45 to 143 s taken directly from the study of Li & Burke (2006) to produce a new 3-D model of the crust and uppermost mantle beneath southern Africa. Abstracting from some of the details, the 3-D model reveals several principal robust characteristics, particularly as they relate to differences in structures beneath the Archean cratons and the marginal Proterozoic provinces. (1) The middle and lower crust is much more homogeneous than the upper crust. (2) Significant lateral variability exists in the upper crust, but the variability is smaller than that observed in non-cratonic regions elsewhere in the world (e.g. California, Yang & Forsyth 2006a). (3) Structural variations in the upper crust tend to be anticorrelated with those in the middle and lower crust, especially in the Kaapvaal craton and the Namaqua-Natal belt. (4) The middle and lower crust is, on average, faster in the Proterozoic provinces than in the Archean cratons. (5) The velocity jump across the Moho is very large across the entire region of study. (6) Crustal thicknesses that we estimate agree well

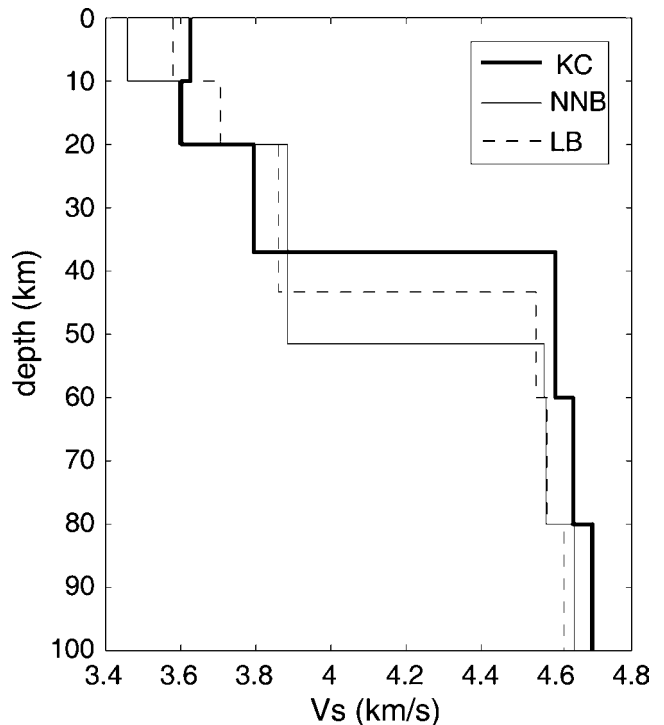


**Figure 14.** Vertical profiles beneath the three grey circles shown in Fig. 11(a): KC, Kaapvaal Craton; NNB, Namaqua-Natal Belt and LB, Limpopo Belt.

with those from the receiver function study of Nair *et al.* (2006), with relatively thicker crust underlying the Proterozoic terranes ( $\sim 43$  km) and thinner crust beneath the undisturbed Archean cratons ( $\sim 37$  km). (7) The upper mantle is, on average, relatively fast beneath the thinner cratonic crust and relatively slow beneath the thicker Proterozoic crust.

Some of these characteristics are succinctly summarized by the vertical profiles plotted in Fig. 14. These profiles are for points beneath the undisturbed Archean Kaapvaal craton, the late-Archean/early-Proterozoic Limpopo Belt north of the Kaapvaal craton and the Proterozoic Namaqua-Natal Belt to its south. The Kaapvaal craton is characterized by a relatively slow, thin lower crust and a fast uppermost mantle. In contrast, the Proterozoic regions have a faster, thicker lower crust and a slower uppermost mantle. This observation is consistent with the study of Durrheim & Mooney (1994) who summarized seismic studies in Africa, Australia, and Eurasia. They found that Proterozoic crust is thick (40–55 km) and has a high velocity layer at its base, while Archean crust is thinner (27–40 km) and lacks the basal high-velocity layer. They conclude that the Archean lower crust is less mafic than in the Proterozoic terranes.

Determination of the cause of this discrepancy between Archean and Proterozoic regions is beyond the scope of this paper. However, if both the Archean cratons and the Proterozoic regions in southern Africa were produced by the assimilation of colliding island arcs, then the model of continental crustal formation by Jull & Keleman (2001) may shed light. They propose a model of the mixing of basaltic and silicic compositions by magma mixing and by partially or completely removing the mafic and ultramafic lower crustal cumulates. Convective instabilities that produce the foundering, however, require high temperatures or low viscosities in the mantle. This appears to pose a problem for the foundering of the Archean lower

crust, which is cold and rigid. However, Behn & Keleman (2006) argue that the lower crust must foundry rapidly in modern arcs. Thus, if the dense lower crust were removed partially or completely in the Archean island arcs prior to their amalgamation to form the craton, the existence of thinner, less mafic crust of the Archean cratons is understandable. If convective instabilities associated with island arc formation and evolution have reduced in vigour as the Earth has cooled, perhaps foundering upon continental crust formation would have been less intense in the Proterozoic than in the Archean. This would explain why the Proterozoic crust is thicker and faster in the basal layer compared to the Archean crust.

Irrespective of its cause, however, the Proterozoic crust appears to be denser than the Archean crust, if the  $V_s$ -to-density conversion is approximately the same in both regions. This is consistent with the gravity study by De Beer & Meyer (1984), which shows that the crust of the Archean province is thinner and less dense by studying gravity profiles across the boundary between the Archean Kaapvaal craton and the Proterozoic Namaqua Province. From the perspective of isostasy, the thinner and less dense crust in the Archean craton will require the upper mantle to compensate the crustal mass deficit in order to preserve isostatic equilibrium given the nearly flat topography.

## ACKNOWLEDGMENTS

We are grateful to Kevin Burke, Cin-Ty Lee and Fenglin Niu for stimulating discussions and helpful comments and to Steve Gao for providing us the crustal model from receiver functions. We gratefully acknowledge two anonymous reviewers and Editor Michael Korn for comments that significantly improved the manuscript. Special thanks go to the seismic group of the Kaapvaal Project for collecting the data and the IRIS Data Management Center for making the data available to us. This work is supported by NSF grant EAR-0450082 and DoE grant DE-FC52–2005NA26607 at the University of Colorado at Boulder and NSF grants EAR-0338430 and EAR-0645503 at the University of Houston.

## REFERENCES

- Barmin, M.P., Ritzwoller, M.H. & Levshin, A.L., 2001. A fast and reliable method for surface wave tomography, *Pure appl. Geophys.*, **158**, 1351–1375.
- Behn, M.D. & Keleman, P.B., 2006. Stability of arc lower crust: insights from the Talkeetna arc section, south central Alaska, and the seismic structure of modern arcs, *J. geophys. Res.*, **111**, doi:10.1029/2006JB004327.
- Bensen, G.D., Ritzwoller, M.H., Barmin, M.P., Levshin, A.L., Lin, F., Moschetti, M.P., Shapiro, N.M. & Yang, Y., 2007a. Processing seismic ambient noise data to obtain reliable broad-band surface wave dispersion measurements, *Geophys. J. Int.*, **169**, 1239–1260.
- Bensen, G.D., Ritzwoller, M.H. & Shapiro, N.M., 2007b. Broad-band ambient noise surface wave tomography across the United States, *J. geophys. Res.*, in press.
- Bensen, G.D., Ritzwoller, M.H. and Yang, Y., 2008. A 3D velocity model of the crust and uppermost mantle beneath the United States from ambient seismic noise, *Geophys. J. Int.*, submitted.
- Chevrot, S. & Zhao, L., 2007. Multiscale finite-frequency Rayleigh wave tomography of the Kaapvaal craton, *J. geophys. Res.*, **112**, 201–215.
- de Beer, J.H. & Meyer, R., 1984. Geophysical characteristics of the Namaqua-Natal Belt and its boundaries, Southern Africa, *J. Geodyn.*, **1**, 473–494.
- de Wit, M.J. & Tinker, J., 2004. Crustal structures across the central Kaapvaal craton from deep-seismic reflection data, *S. Afric. J. Geol.*, **107**, 185–206.
- de Wit, M.J. *et al.*, 1992. Formation of an Archean continent, *Nature*, **357**, 553–562.
- Durrheim, R.J. & Green, R.W.E., 1992. A seismic refraction investigation of the Archean Kaapvaal Craton, South Africa, using mine tremors as the energy source, *Geophys. J. Int.*, **108**, 812–832.
- Durrheim, R.J. & Mooney, W.D., 1991. Archean-Archean and Proterozoic crustal evolution: evidence from crustal seismology, *Geology*, **19**, 606–609.
- Durrheim, R.J. & Mooney, W.D., 1994. Evolution of the Precambrian lithosphere: seismological and geochemical constraints, *J. geophys. Res.*, **99**, 15 359–15 374.
- Ekstrom, G., Tromp, J. & Larson, E.W., 1997. Measurements and global models of surface wave propagation, *J. geophys. Res.*, **102**, 8137–8157.
- Forsyth, D.W. & Li, A., 2005. Array-analysis of two-dimensional variations in surface wave phase velocity and azimuthal anisotropy in the presence of multi-pathing interference, in *Seismic Earth: Array Analysis of Broadband Seismograms*, Geophys. Monogr. Ser., Vol. 157, eds A. Levander & G. Nolet, pp. 81–97, AGU, Washington, DC.
- Forsyth, D.W., Webb, S., Dorman, L. & Shen, Y., 1998. Phase velocities of Rayleigh waves in the MELT experiment on the East Pacific Rise, *Science*, **280**, 1235–1238.
- Fouch, M.J., James, D.E., Van Decar, J.C., Van Der Lee, S. & Kaapvaal Seismic Group 2004. Mantle seismic structure beneath the Kaapvaal and Zimbabwe cratons, *S. Afric. J. Geol.*, **107**, 33–44.
- Grand, S.P., Van Der Hilst, R.D. & Widiyantoro, S., 1997. Global seismic tomography: a snapshot of convection in the Earth, *GSA Today*, **7**, 1–7.
- Green, R.W.E. & Durrheim, R.J., 1990. A seismic refraction investigation of the Namaqualand metamorphic complex, South Africa, *J. geophys. Res.*, **95**, 19927–19932.
- Herrmann, R., 1987. *Computer Programs in Seismology*, Saint Louis University, St. Louis, Missouri.
- Holbrook, W.S., Mooney, W.D. & Christensen, N.I., 1992. The seismic velocity structure of the deep continental crust, in *Continental Lower Crust*, pp. 1–43, eds D.M. Fountain, R. Arculus & R.W. Kay, Elsevier, Amsterdam, the Netherlands.
- James, D.E., Fouch, M.J., VanDecar, J.C., Van Der Lee, S. & the Kaapvaal Seismic Group, 2001. Tectospheric structure beneath southern Africa, *Geophys. Res. Lett.*, **28**, 2485–2488.
- Jordan, T.H., 1979. Mineralogies, densities, and seismic velocities of garnet lherzolites and their geophysical implications, in *The Mantle Sample: Inclusions in Kimberlites and Other Volcanics Proceedings of the Second International Kimberlite Conference*, pp. 1–14, eds F.R. Boyd & Meyer, H.O.A., AGU, Washington, DC, United States.
- Jordan, T.H., 1988. Structure and formation of the continental tectosphere, *J. Petrol.*, Special Lithosphere issue, 11–37.
- Jull, M. & Keleman, P.B., 2001. On the conditions for the lower crustal convective instability, *J. geophys. Res.*, **106**, 6423–6446.
- Kang, T.-S. & Shin, J.S., 2006. Surface-wave tomography from ambient seismic noise of accelerograph networks in southern Korea, *Geophys. Res. Lett.*, **33**, L17303, doi:10.1029/2006GL027044.
- Kennett, B.L.N., Engdahl, E.R. & Buland, R., 1995. Constraints on seismic velocities in the Earth from travel times, *Geophys. J. Int.*, **122**, 108–124.
- Levshin, A.L., Barmin, M.P., Ritzwoller, M.H. & Trampert, J., 2005. Minor arc and major-arc global surface wave diffraction tomography, *Phys. Earth planet. Int.*, **149**, 205–223.
- Li, A. & Burke, K., 2006. Upper mantle structure of southern Africa from Rayleigh wave tomography, *J. geophys. Res.*, **111**, B10303, doi:10.1029/2006JB004321.
- Li, A., Forsyth, D.W. & Fischer, K.M., 2003. Shear velocity structure and azimuthal anisotropy beneath eastern North America from Rayleigh wave inversion, *J. geophys. Res.*, **108**, 2362, doi:10.1029/2002JB002259.
- Lin, F., Ritzwoller, M.H., Townend, J., Savage, M. & Bannister, S., 2007a. Ambient noise Rayleigh wave tomography of New Zealand, *Geophys. J. Int.*, **170**(2), 649–666.
- Lin, F., Moschetti, M.P. & Ritzwoller, M.H., 2008. Surface wave tomography of the western United States from ambient seismic noise: Rayleigh and Love wave phase velocity maps, *Geophys. J. Int.*, doi:10.1111/j1365-246X.2008.03720.x.

- Lobkis, O.I. & Weaver, R.L., 2001. On the emergence of the Green's function in the correlations of a diffuse field. *J. Acoust. Soc. Am.*, **110**, 3011–3017.
- Moschetti, M.P., Ritzwoller, M.H. & Shapiro, N.M., 2007. Surface wave tomography of the western United States from ambient seismic noise: Rayleigh wave group velocity maps, *Geochem., Geophys., Geosys.*, **8**, Q08010, doi:10.1029/2007GC001655.
- Nair, S.K., Gao, S.S., Liu, K.H. & Silver, P.G., 2006. Southern African crustal evolution and composition: constraints from receiver function studies, *J. geophys. Res.*, **111**, B02304, doi:10.1029/2005JB003802.
- Nguuri, T. *et al.*, 2001. Crustal structure beneath southern Africa and its implications for the formation and evolution of the Kaapvaal and Zimbabwe cratons, *Geophys. Res. Lett.*, **28**, 2501–2504.
- Ritsemá, J. & van Heijst, H., 2000. New seismic model of the upper mantle beneath Africa, *Geology*, **28**, 63–66.
- Roux, P., Sabra, K.G., Kuperman, W.A. & Roux, A., 2005. Ambient noise cross correlation in free space: theoretical approach, *J. Acoust. Soc. Am.*, **117**, 79–84.
- Saito, M., 1988. DISPER80: a subroutine package for the calculation of seismic normal-mode solutions, in *Seismological Algorithms*, pp. 293–319, ed. D.J. Doornbos, Elsevier, New York.
- Shapiro, N.M. & Ritzwoller, M.H., 2002. Monte-Carlo inversion for a global shear velocity model of the crust and upper mantle, *Geophys. J. Int.*, **151**, 88–105.
- Shapiro, N.M., Ritzwoller, M.H., Molnar, P. & Levin, V., 2004. Thinning and flow of Tibetan crust constrained by seismic anisotropy, *Science*, **305**, 233–236.
- Shapiro, N.M., Campillo, M., Stehly, L. & Ritzwoller, M.H., 2005. High resolution surface wave tomography from ambient seismic noise, *Science*, **307**, 1615–1618.
- Snieder, R., 2004. Extracting the Green's function from the correlation of coda waves: a derivation based on stationary phase, *Phys. Rev. E*, **69**, 046610.
- Tinker, J., de Wit, M. & Grotzinger, J., 2002. Seismic stratigraphic constraints on Neoproterozoic–Paleoproterozoic evolution of the western margin of the Kaapvaal craton, South Africa, *S. Afric. J. Geol.*, **105**, 107–134.
- Villaseñor, A., Yang, Y., Ritzwoller, M.H. & Gallart, J., 2007. Ambient noise surface wave tomography of the Iberian Peninsula: implications for shallow seismic structure, *Geophys. Res. Lett.*, **34**, L11304, doi:10.1029/2007GL030164.
- Webb, S.J., Cawthorn, R.G., Nguuri, T. & James, D., 2004. Gravity modeling of Bushveld Complex connectivity supported by Southern African Seismic Experiment results, *S. Afric. J. Geol.*, **107**, 207–218.
- Weeraratne, D.S., Forsyth, D.W., Yang, Y. & Webb, S.C., 2007. Rayleigh wave tomography of the upper mantle beneath intraplate seamount chains in the south Pacific, *J. geophys. Res.*, **112**, B06303, doi:10.1029/2006JB004403.
- Yang, Y. & Forsyth, D.W., 2006a. Rayleigh wave phase velocities, small-scale convection and azimuthal anisotropy beneath southern California, *J. geophys. Res.*, **111**, B07306, doi:10.1029/2005JB004180.
- Yang, Y. & Forsyth, D.W., 2006b. Regional tomographic inversion of amplitude and phase of Rayleigh waves with 2-D sensitivity kernels, *Geophys. J. Int.*, **166**, 1148–1160.
- Yang, Y. & Ritzwoller, M.H., 2008. The characteristics of ambient seismic noise as a source for surface wave tomography, *Geochem., Geophys., Geosys.*, **9**(2), Q02008, doi:10.1029/2007GC001814.
- Yao, H., Van Der Hilst, R.D. & De Hoop, M.V., 2006. Surface-wave array tomography in SE Tibet from ambient seismic noise and two-station analysis: I—Phase velocity maps, *Geophys. J. Int.*, **166**, 732–744.
- Yang, Y., Ritzwoller, M.H., Levshin, A.L. & Shapiro, N.M., 2007. Ambient noise Rayleigh wave tomography across Europe, *Geophys. J. Int.*, **168**, 259–274.
- Zandt, G. & Ammon, C.J., 1995. Continental crust composition constrained by measurements of crustal Poisson's ratio, *Nature*, **374**, 152–154.